Title

Unsupervised Classification of Interictal Intracranial Electroencephalography Activity as Pathological or Physiological in Epilepsy Patients

Author

Bentaleb, Soulaimane

Publication Date

2024

Peer reviewed|Thesis/dissertation

UNIVERSITY OF CALIFORNIA

Los Angeles

Unsupervised Classification of Interictal Intracranial Electroencephalography Activity as Pathological or Physiological in Epilepsy Patients

A thesis submitted in partial satisfaction

of the requirements for the degree

Master of Science in Bioengineering

by

Soulaimane Bentaleb

2024

ABSTRACT OF THE THESIS

Unsupervised Classification of Interictal Intracranial Electroencephalography Activity as Pathological or Physiological in Epilepsy Patients

by

Soulaimane Bentaleb

Master of Science in Bioengineering

University of California, Los Angeles, 2024

Professor Wentai Liu, Chair

With timely and proper treatment, an estimated 70% of the 65 million people with epilepsy worldwide could be seizure-free. For the 30-40% of epilepsy patients who do not respond to anti-seizure drugs, detection of pathological interictal activity can speed up treatment procedures. However, analysis of brain activity is a manual process today, which is tedious, time-consuming, and unscalable. An automated approach tackles these issues. That said, interictal detection algorithms rely on supervised learning, which requires labeled training data and human intervention for patient-specific tuning. An unsupervised approach overcomes these limitations with an automated and

personalized solution that requires no labels or intervention from medical staff. The algorithm presented in this thesis is a fully unsupervised model that classifies intracranial electroencephalography (iEEG) interictal activity as pathological or physiological. 170 features were extracted from three domains: time (19 features), frequency (7 features), and time-frequency (144 features). Four unsupervised dimensionality reduction techniques were then combined with four unsupervised classification methods. Out of these 16 combinations, Principal Component Analysis (PCA) paired with a K-Means model achieved the best performance. Across 15 epilepsy patients, it yielded an average 92.6% F-2 score, 93.5% precision, and 93.0% recall with standard deviations of 12.0%, 13.8%, and 12.5%, respectively. There was no statistically significant difference between the performance of this unsupervised model and that of two supervised models, Support Vector Machine and Random Forest. The proposed method is a promising approach to enhancing the efficiency of treatment for drug-resistant epilepsy.

The thesis of Soulaimane Bentaleb is approved.

William F. Speier

Corey Wells Arnold

Nanthia A. Suthana

Wentai Liu, Committee Chair

University of California, Los Angeles

2024

To my parents, brothers, family, and friends

Thank you for everything

Table of Contents

List of Figures

List of Tables

Acknowledgments

I would like to thank Dr. Wentai Liu for supporting my research project. I would also like to thank Han Xu for his advice, guidance, and meaningful contribution to this work.

Han Xu developed the simulation algorithm used to validate my classification model and wrote the sections II. H. 3. i-v that explain how the algorithm works and how the simulated dataset was generated. These sections were expanded and adapted to fit into this thesis.

I. Introduction

Epilepsy is a neurological disorder characterized by repeated seizures. A seizure is a burst of abnormal electrical activity in the brain. Epilepsy is the fourth most common neurological disorder in the United States and the world, with 3.5 and 65 million people actively suffering from the condition, respectively.[1] If they are properly and timely diagnosed and treated, the World Health Organization (WHO) estimates that 70% of these epilepsy patients could become seizure-free.[2] The first treatment option for patients diagnosed with epilepsy is anti-seizure drugs. However, only 60 to 70% of patients respond to these medications (Figure 1).[3] The most common treatment for patients with drug-resistant epilepsy is surgical resection of the Seizure Onset Zone (SOZ). The other option for these 30 to 40% of epilepsy patients is implantable neurostimulation devices.

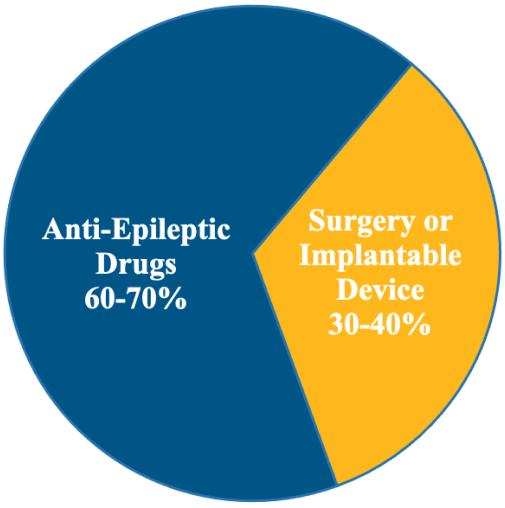

Figure 1. Pie chart of epilepsy treatment options. 60-70% of epilepsy patients are treated with anti-epileptic drugs. Surgical resection of the seizure onset zone and implantable devices are the two treatment options for the 30-40% of patients who do not respond to anti-seizure medications.

Electroencephalography (EEG), which records the brain's electrical signals, is the most common tool to study epilepsy for clinical and research purposes.[4] To prepare for surgical resection or device placement, patients are implanted with intracranial EEG (iEEG) electrodes and spend several days at the hospital for Video-EEG Monitoring (VEM). The hospital length of stay is one week on average but can range from 3 to 14 days.[5,6] The clinical gold standard is the visual inspection of the data by trained neurologists to manually identify seizures, also called ictal activity.[7] It is thus impossible to look at all of the recorded data. Instead, a nurse continuously monitors the patient with VEM and makes note when they recognize that the patient is having a seizure.[8] Only the iEEG data that the nurse flags are then analyzed by epileptologists to look for seizures. Days' worth of interictal data, between seizure episodes, are thus never looked at although the detection of interictal pathological activity can also be used to localize the SOZ and identify the brain area to be surgically removed or implanted with a neurostimulation device.[9,10] One of the biomarkers of interictal pathological activity, high-frequency oscillations (HFOs), was proven clinically relevant for epileptic surgery by a 2017 study.[11] iEEG electrodes with high rates of HFOs defined the HFO area, which was fully resected in all 13 patients who achieved seizure freedom post-surgery, resulting in 100% specificity. As for the remaining 7 patients, who all had recurrent seizures post-surgery, the resection of the HFO area may have improved the outcome for 4 of them, as the HFO area was partially resected in 4 patients (100% positive predictive value and 57% sensitivity) and fully resected in 3 patients (81% negative predictive value).

Several pathological electrophysiological biomarkers were proven effective for detecting interictal epileptic iEEG activity, including HFOs and interictal epileptiform discharges (IEDs).[12] Manual detection of this activity is tedious, time-consuming, and unscalable.[13] Automatic detection methods solve these problems (Table 1). Unfortunately, existing interictal detection algorithms rely on supervised learning, which requires a large, labeled training dataset and careful human intervention for patient-specific tuning, as it yields a general model that is the same for all patients.[14] An unsupervised approach overcomes these limitations as it requires no labels and offers a unique and personalized option specific to each new patient by training on each patient's brain data independently.[14]

Manual Detection	**Automatic Supervised Detection**	**Automatic Unsupervised Detection**
• Tedious • Time-consuming • Unscalable	• Requires large, labeled training dataset • Is the same for all patients	• Does not require labels • Is personalized and unique to each patient

Table 1. Characteristics of pathological activity detection methods.

The proposed model achieved fully unsupervised classification of iEEG interictal activity as pathological or physiological in epilepsy patients. It is a pre-labeling algorithm aimed as a complementary aid for neurologists that takes advantage of all of the data recorded from a patient during VEM. Rather than never looking at days' worth of interictal data, neurologists could now look at the data segments this model pre-labels as pathological. This would empower them to make the final decision on the epileptic

nature of the data and provide additional valuable information to identify the SOZ faster and make the patient's length of stay shorter.

II. Materials and Methods

A. Dataset

The dataset analyzed in this paper was collected from 25 epilepsy patients at the Mayo Clinic (Rochester, Minnesota, USA).[15] The iEEG data were collected from each patient from 1:00 am to 3:00 am the first night after they were implanted with either grids and strips, depth electrodes, or both. The data were acquired at a 32 kHz sampling rate using a hardware bandpass filter from DC to 9 kHz. The data were then down-sampled to 5 kHz and split into 3-second segments, each containing 15,000 iEEG data points. Three reviewers annotated each segment as one of four labels: power line noise, muscle and machine artifacts, pathological/epileptic activity, or physiological/healthy activity. In this dataset, pathological activity was defined as a signal with epileptiform graphoelements, such as HFOs, spikes, or IEDs. The 3-second length was selected empirically as muscle artifacts spanned over multiple seconds and 3 seconds provided sufficient context to differentiate between the four classes. The dataset contained 155,182 total segments (Table 2). Only the segments labeled as pathological or physiological were kept. Since all segments for 10 patients were power line noise or muscle and machine artifacts, the final number of patients and segments was 15 and 71,957, respectively. 56,730 segments were physiological and 15,227 were pathological.

Classification category	Number of segments
Physiological activity	56,730
Pathological activity	15,227
Artifacts	41,303
Power line noise (60 Hz)	41,922
Total	155,182

Table 2. Number of 3-second segments for each classification category.

B. Time Analysis

Three raw physiological segments (Figure 2A) and three raw pathological segments (Figure 2B), all randomly selected, were plotted in the time domain for data visualization purposes. Focusing on the signals in the first row, the key difference between the two segments was the high-amplitude peak at 1.5 seconds reaching a maximum voltage of 6 μV in the pathological signal, whereas the physiological signal had a consistent voltage ranging from -2 to 2 μV throughout the 3 seconds. This distinction was also present in the second and third rows' signals and was confirmed by plotting several other physiological and pathological segments and observing similar characteristics.

The physiological and pathological segments from the first row were used to perform the frequency and time-frequency analyses.

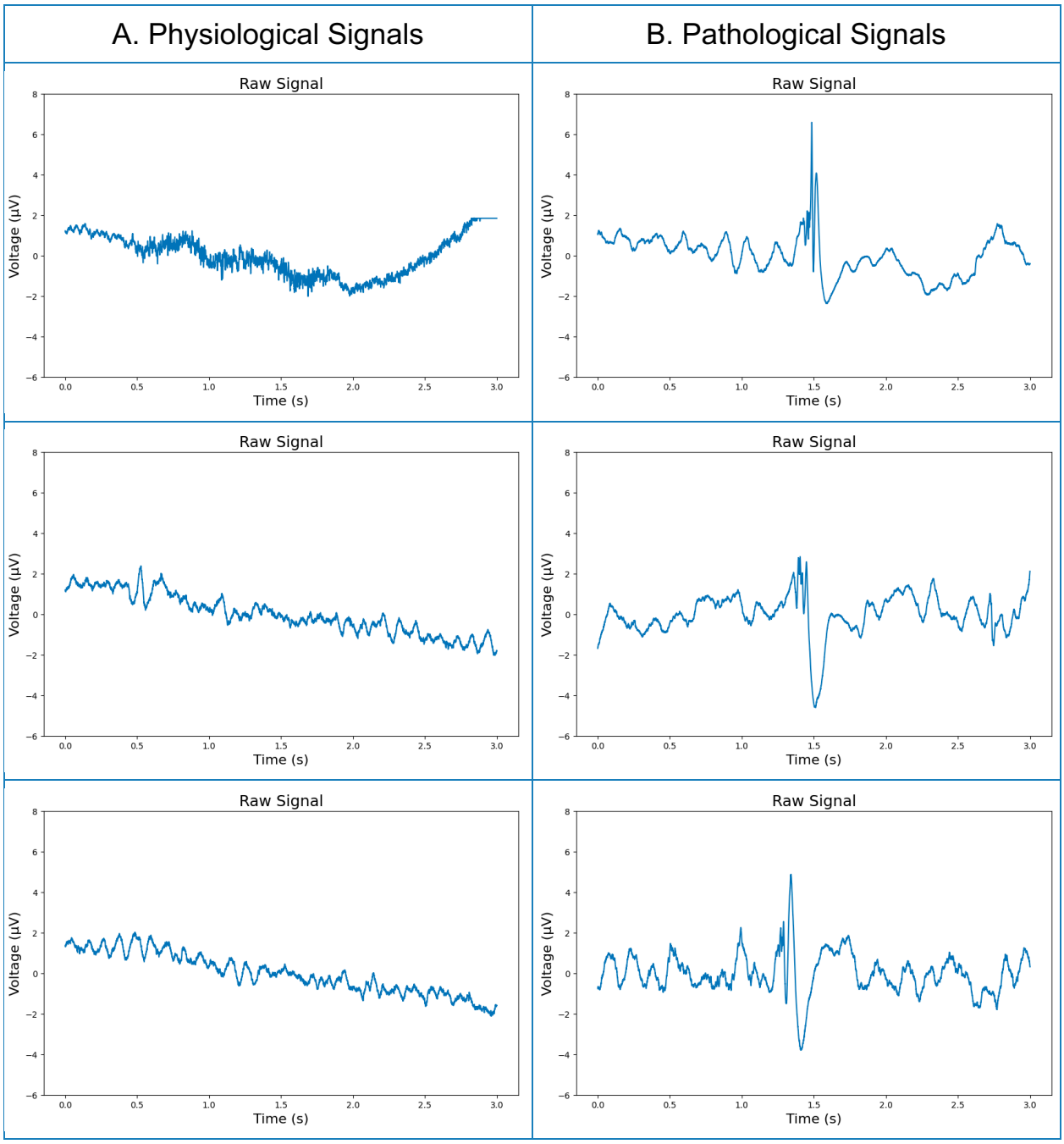

Figure 2. Plots of three raw iEEG physiological signals (A) and three pathological signals (B) in the time domain.

C. Frequency Analysis

The Power Spectral Densities (PSD) of the physiological and pathological segments were plotted in the five major frequency bands: delta (1-4 Hz), theta (4-8 Hz), alpha (8-13 Hz), beta (13-30 Hz), and gamma (30-80 Hz) (Figure 3). The PSD represents the power distribution of the frequency components obtained by taking the Discrete Fourier Transform (DFT) of a signal using the Fast Fourier Transform (FFT) [Equation 1].[16] The PSD is computed by dividing the discrete-time signal into successive blocks and averaging the mean squared amplitude of the DFT of these blocks [Equation 2].[17]

$$X_k = \sum_{n=0}^{N-1} x_n \cdot e^{-i2\pi kn/N} \qquad \text{[Equation 1]}$$

Where x_n is the discrete-time signal at sample n, X_k is the DFT, which includes both amplitude and phase, N is the number of samples, n is the current sample, and k is the current frequency, which ranges from 0 to N-1, inclusive.

$$\hat{R}_x(\omega_k) = \frac{1}{M} \sum_{m=0}^{M-1} |DFT_k(x_m)|^2 \qquad \text{[Equation 2]}$$

Where $x_m(n) = x(n + mN)$, with $n = 0, 1, \ldots, N-1$, is the m^{th} signal block and M is the number of blocks.

The time-domain distinction manifests itself in the frequency domain as well. Figure 3 shows the PSD difference between the physiological and pathological signals,

which is more visible on a logarithmic scale in Figures 3C and 3D. The physiological signal's PSD exceeds 0.005 W/Hz in the delta band only, where it reaches 0.075 W/Hz (Figure 3A). However, the pathological signal's PSD reaches 0.6 W/Hz in the delta band, 0.28 W/Hz in the theta band, 0.05 W/Hz in the alpha band, and 0.025 W/Hz in the beta and gamma bands (Figure 3B).

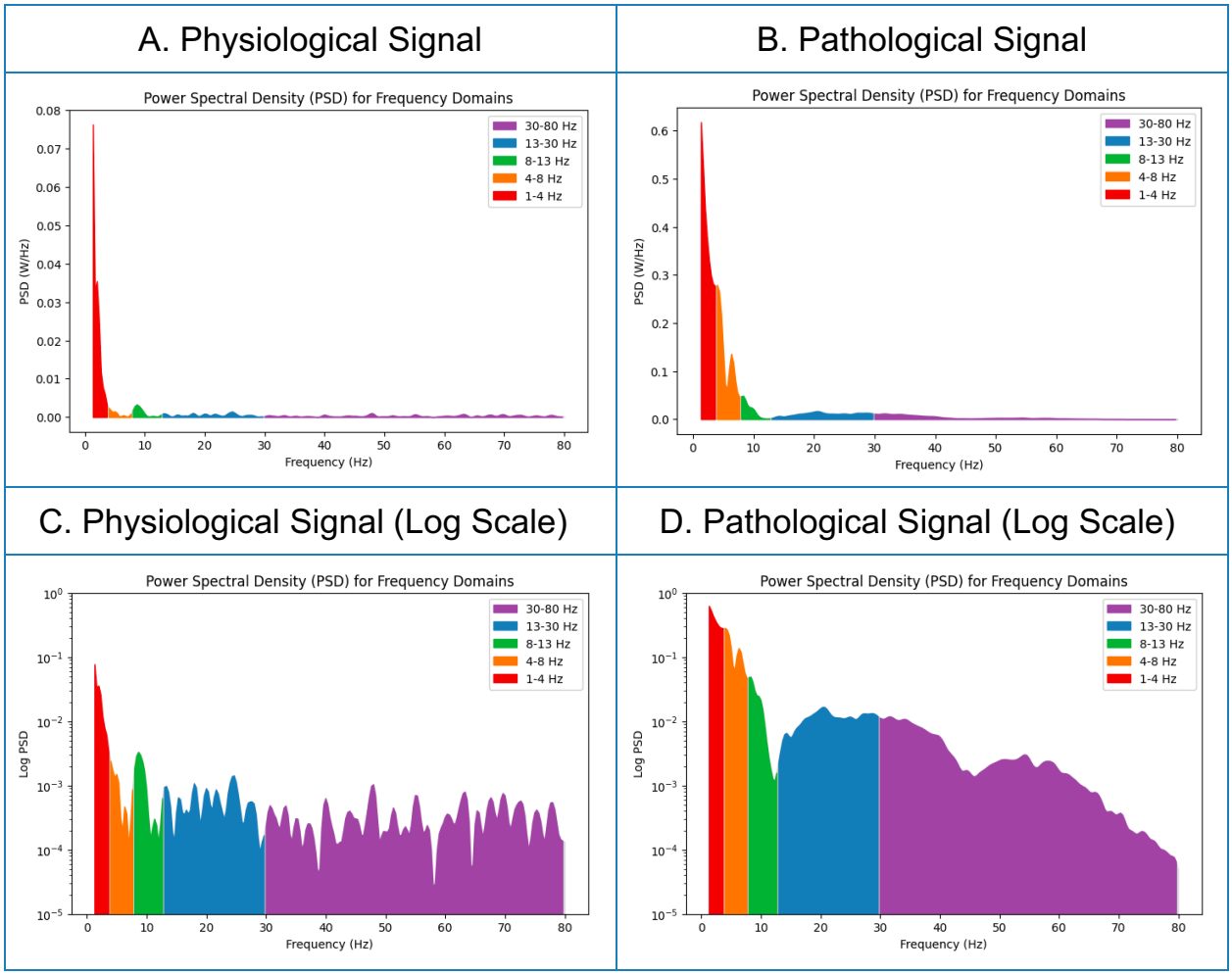

Figure 3. Plots of the Power Spectral Density (PSD) of the iEEG physiological signal (A) and pathological signal (B) in the five major frequency bands: delta (1-4 Hz), theta (4-8 Hz), alpha (8-13 Hz), beta (13-30 Hz), and gamma (30-80 Hz). Plots of the PSD on a logarithmic scale for the physiological signal (C) and pathological signal (D).

D. Time-Frequency Analysis

To calculate a signal's DFT, it is assumed that the signal is stationary, meaning that its statistical properties are time-independent and do not change in time. However, an EEG signal is the sum of the electrical activity of 30-500 million neurons.[18] The brain processes underlying the activity of these neurons have properties that vary over time, so EEG signals are non-stationary.[19] The DFT was still used in the frequency analysis to compute the PSD because the analyzed segment was only 3 seconds long and it is possible to assume that a non-stationary signal is quasi-stationary by dividing it into short windows. The PSD plots yielded valuable frequency-domain information consistent with the time-domain observations. That being said, the physiological and pathological segments were also inspected in the time-frequency domain to perform a more accurate assessment. Three signal processing methods were compared to select the best time-frequency analysis technique.

1. Short-Time Fourier Transform

The Short-Time Fourier Transform (STFT) analyzes a non-stationary signal by segmenting it into windows and computing the FFT of each window [Equation 3].[20] Therefore, the STFT provides equally spaced time-frequency localization.

$$X_{STFT}[m,n] = \sum_{k=0}^{L-1} x[k]g[k-m]e^{-j2\pi nk/L} \qquad \text{[Equation 3]}$$

Where x[k] is the discrete-time signal and g[k] is an L-point window function.

The STFT was used to create spectrograms representing the signal's frequencies as a function of time for the physiological and pathological segments (Figure 4). The STFT was computed using 0.5-second windows with the Hann window function and 0.375-second overlap. The plots show the peak present in the pathological signal at 1.5 seconds, which has high-frequency components that contrast with the low frequencies present in the rest of the pathological segment and present throughout the whole physiological segment. In the physiological signal, no frequency components above 5 Hz had a magnitude higher than 40 dB whereas in the pathological signal, frequency components with a magnitude higher than 40 dB were present from 0 to 15 Hz throughout the segment and reached 70 Hz between 1.375 and 1.750 seconds due to the peak.

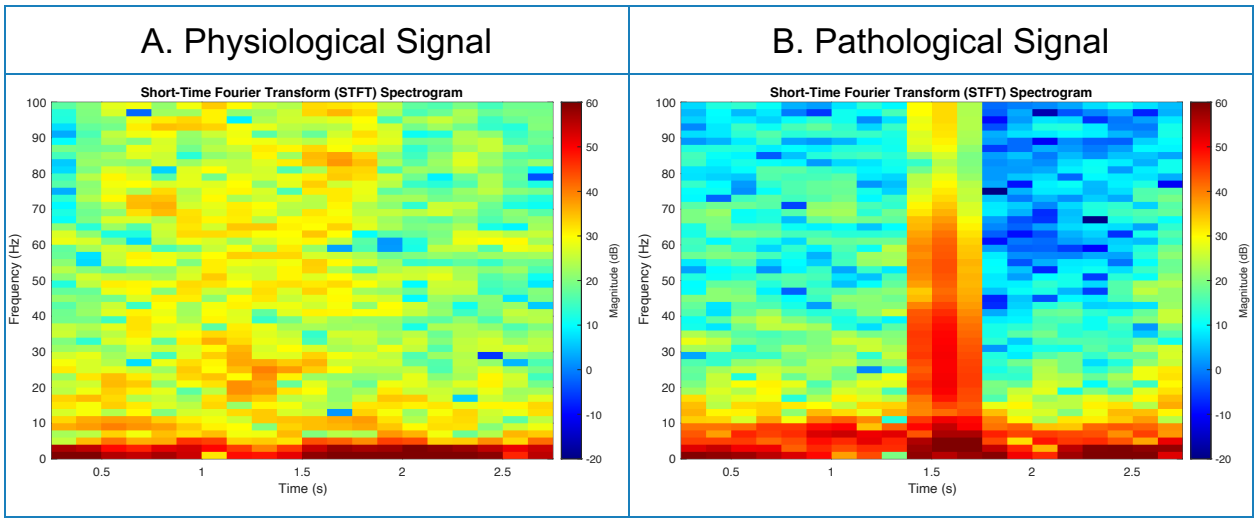

Figure 4. Plots of the Short-Time Fourier Transform (STFT) spectrograms of the iEEG physiological signal (A) and pathological signal (B).

2. Hilbert-Huang Transform

The Hilbert-Huang Transform (HHT) uses two steps to analyze a non-linear and non-stationary signal: Empirical Mode Decomposition (EMD) and Hilbert Transform (HT). The EMD was used to decompose the physiological and pathological segments into Intrinsic Mode Functions (IMFs), which are simpler components of the raw signal that allow the HHT to handle non-stationary signals. The sum of all IMFs reconstructs the raw signal [Equation 4].[21] Figure 5 shows the 9 IMFs that compose the pathological segment.

$$x(t) = \sum_{i=0}^{n} c_i(t) + r_n(t) \qquad \text{[Equation 4]}$$

Where x(t) is the continuous-time signal, $c_i(t)$ is the i^{th} IMF, and $r_n(t)$ is the residue.

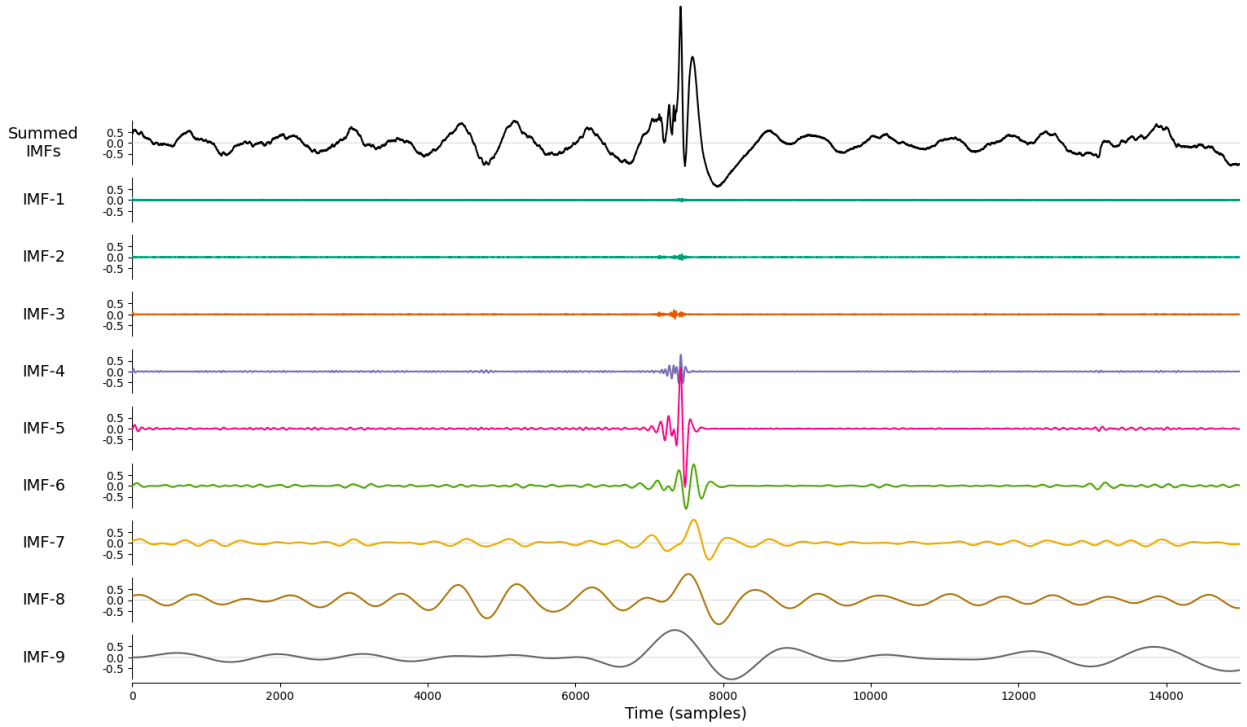

Figure 5. Pathological signal and all of its intrinsic mode functions (IMFs).

The HT of each IMF was computed to construct the HHT time-frequency spectrograms [Equation 5].[22] The plots are mostly white because they are sparse, as they indicate the frequency components of each IMF over time (Figure 6). The spectrograms display the peak in the pathological signal, as the frequency reaches 60 Hz with a magnitude of 12 dB, whereas all other frequency components do not exceed 2 dB in the rest of the pathological segment and in the entire physiological segment.

$$y_i(t) = \frac{1}{\pi}\int_{-\infty}^{+\infty} \frac{c_i(\tau)}{t-\tau}\, d\tau \qquad \text{[Equation 5]}$$

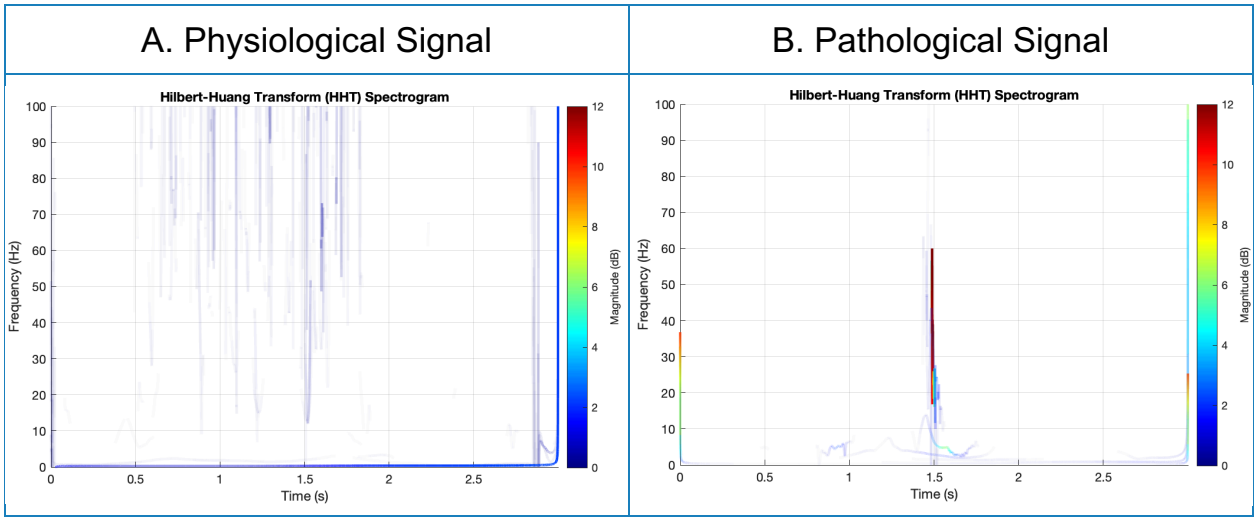

Figure 6. Plots of the Hilbert-Huang Transform (HHT) spectrograms of the iEEG physiological signal (A) and pathological signal (B).

3. Wavelet Transform

The Wavelet Transform (WT) decomposes a signal into a set of wavelets by convolving it with a mother wavelet function. In contrast to the STFT, the WT is characterized by high frequency resolution at low frequencies and high time resolution

at high frequencies. Although the iEEG signals are all discrete-time, the Continuous Wavelet Transform (CWT) is easier to interpret than the Discrete Wavelet Transform (DWT) as there is significant overlap between wavelets at each scale and between scales in the CWT [Equation 6].[23] This redundancy makes the signal properties easier to read.

$$X_w(a,b) = \frac{1}{|a|^{1/2}} \int_{-\infty}^{\infty} x(t)\overline{\psi}\left(\frac{t-b}{a}\right) dt \qquad \text{[Equation 6]}$$

Where $X_w(a,b)$ are the wavelet coefficients, x(t) is the continuous-time signal, $\bar{\psi}$ is the complex conjugate of the mother wavelet, a is the scale parameter, and b is the translation parameter.

The CWT using the Analytic Morlet (Gabor) Wavelet function produced the spectrograms of the physiological and pathological segments (Figure 7). The pathological signal's plot displays a large contrast between the peak at 1.5 seconds and both the rest of the pathological segment and the physiological signal. The peak's frequency reached 100 Hz with a magnitude ranging from 0.5 to 1.5 dB, whereas the rest of the pathological signal had no frequency components exceeding a 0.6 dB magnitude and the physiological segment had no frequency components exceeding a 0.35 dB magnitude.

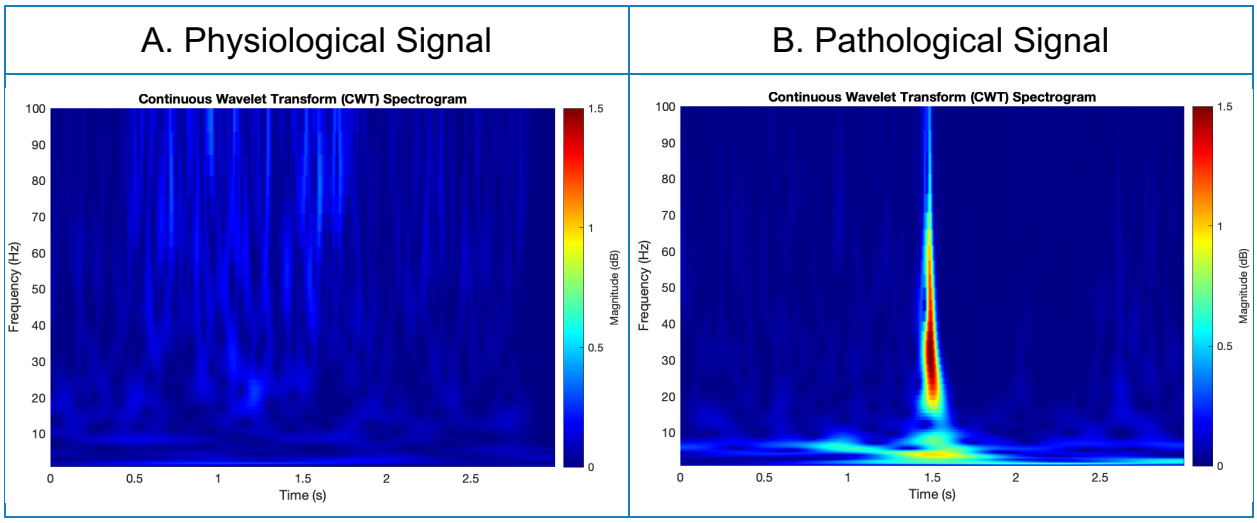

Figure 7. Plots of the Continuous Wavelet Transform (CWT) spectrograms of the iEEG physiological signal (A) and pathological signal (B).

4. Comparison

Based on careful observation of the spectrograms yielded by the three time-frequency analysis methods, the wavelet transform was the best signal processing technique to analyze this dataset. It most accurately represented the peak present in the pathological signal and showed the greatest contrast with the rest of the pathological segment and with the physiological signal.

E. Feature Extraction

1. Complex Statistical Features in the Time Domain

The 19 complex statistical features categorized in Table 3 were extracted from each raw iEEG segment in the time domain.[24,25]

Categories	Features
Entropy	Attention entropy
	Bubble entropy
	Conditional weighted permutation entropy
	Multiscale permutation entropy
	Singular value decomposition entropy
Multifractal detrended fluctuation analysis	Width of the multifractal singularity spectrum
	Peak: the value of the singularity exponent corresponding to the peak of the singularity dimension
	Mean of the maximum and minimum values of the singularity exponent
	Max: the value of the multifractal singularity spectrum corresponding to the maximum value of the singularity exponent
	Delta: the vertical distance between the singularity spectrum where the singularity exponents are at their max and min
	Asymmetric ratio corresponding to the centrality of the peak of the multifractal singularity spectrum
	Fluctuation of the generalized Hurst's exponents
	Increment: cumulative function index of the squared increments of the generalized Hurst's exponents
Line length	Line length
	Fractal line length

Hjorth	Hjorth's complexity
	Hjorth's mobility
	Hjorth's activity
Other	Nonlinear energy

Table 3. The 19 complex statistical features extracted from each raw iEEG segment in the time domain and their corresponding categories.

2. Features in the Frequency Domain

The 7 features categorized in Table 4 were extracted from each iEEG segment in the frequency domain.

Categories	Features
Power Spectral Density (PSD) in the 5 major frequency bands	PSD in the Delta band (1-4 Hz)
	PSD in the Theta band (4-8 Hz)
	PSD in the Alpha band (8-13 Hz)
	PSD in the Beta band (13-30 Hz)
	PSD in the Gamma band (30-80 Hz)
Intensity-weighted features	Intensity-weighted mean frequency
	Intensity-weighted bandwidth

Table 4. The 7 features extracted from each iEEG segment in the frequency domain and their corresponding categories.

3. Simple Statistical Features from Discrete Wavelet Transform Coefficients in the Time-Frequency Domain

Since every iEEG segment in the dataset was a discrete-time signal, it was important to use the DWT rather than the CWT for feature extraction. The DWT computes two sets of coefficients from the raw signal: approximation coefficients and detail coefficients [Equation 7].[26] Approximation coefficients are the output of a low-pass filter, which serves as an averaging filter, whereas detail coefficients are the output of a high-pass filter, which serves as a difference filter.

$$W_\varphi[j_o,k] = \frac{1}{\sqrt{M}} \sum_n x[n]\varphi_{j0,k}[n]$$
$$W_\psi[j,k] = \frac{1}{\sqrt{\mathrm{M}}} \sum_n x[n]\psi_{j,k}[n] \quad \text{for } j \geq j_0$$

[Equation 7]

Where x[n] is the discrete-time signal, $W_\varphi[j_0,k]$ are the approximation coefficients, $W_\psi[j,k]$ are the detail coefficients, n = 0, 1, 2, …, M-1, j = 0, 1, 2, …, J-1, k = 0, 1, 2, …, 2^j-1, and M is the number of samples to be transformed and equals 2J, where J indicates the number of transform levels. The basis functions $\varphi_{j,k}[n]$ and $\psi_{j,k}[n]$ are the scaling function and wavelet function, respectively [Equation 8].[26]

$$\varphi_{j,k}[n] = 2^{j/2}\varphi\left[2^j n - k\right]$$
$$\psi_{j,k}[n] = 2^{j/2}\psi\left[2^j n - k\right]$$

[Equation 8]

The optimal wavelet function to use was determined by applying the DWT as a low-pass filter and observing which wavelet function removed high-frequency noise while retaining the peak in the pathological signal. Figure 8 shows a snapshot of this

process, where the original pathological signal and the DWT-filtered signal were superimposed after applying the commonly used first-order Daubechies wavelet function (Figure 8A) or the first-order Coiflets wavelet function (Figure 8B). The latter yielded a low-pass filtered signal that successfully retained the pathological peak, whereas the former removed the high-frequency components of the peak, which decreased its amplitude. This distinction was confirmed by using several other wavelet functions and making the same observation. The first-order Coiflets wavelet function was thus selected for feature extraction.

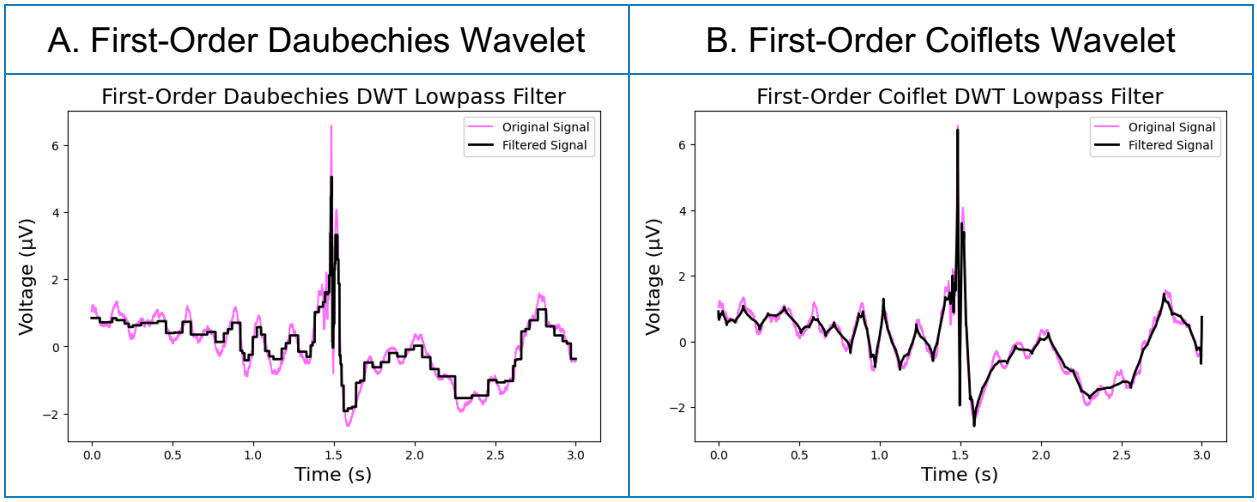

Figure 8. Plots of the original and Discrete Wavelet Transform (DWT) low-pass filtered pathological signal using the first-order Daubechies wavelet (A) and the first-order Coiflets wavelet (B).

For each iEEG segment, the DWT was applied using the first-order Coiflets wavelet function to return 12 arrays of approximation and detail coefficients. The 12 simple statistical features categorized in Table 5 were extracted from each of the 12 coefficient arrays to yield 144 features in the time-frequency domain.

Categories	Features
Common statistics	Mean
	Median
	Variance
	Standard deviation
Percentiles	5^{th} percentile
	25^{th} percentile
	75^{th} percentile
	95^{th} percentile
Crossings	Zero crossings (number of times a signal crosses y = 0)
	Mean crossings (number of times a signal s crosses y = mean(s))
Other	Entropy
	Root mean square (square root of the average of the squared amplitude values)

Table 5. The 12 simple statistical features extracted from each of the 12 DWT arrays of coefficients from each iEEG segment in the time-frequency domain and their corresponding categories.

The 170 overall features calculated from each segment's time (19 features), frequency (7 features), and time-frequency domains (144 features) were concatenated into an array.

F. Dimensionality Reduction

Dimensionality reduction methods reduce the dimensionality of a feature set while preserving most of its variance. Principal Component Analysis (PCA) is the most commonly used statistical technique to accomplish this. It transforms the original features into a new set of uncorrelated variables, called principal components, which are linear combinations of the original features that result in the maximum variance in the feature set. These components are ordered by the amount of variance they contain, with the first component containing the most variance and the last one explaining the least variance (Figure 9A).

To determine the number of principal components used by the dimensionality reduction methods in this thesis, a threshold of 90% was set for the cumulative variance contained by principal components using PCA (Figure 9B). This threshold resulted in 39 principal components, which explained 90.3% of the variance. This analysis was also performed with Singular Value Decomposition (SVD), which yielded the same result of 39 principal components, containing 90.3% of the variance.

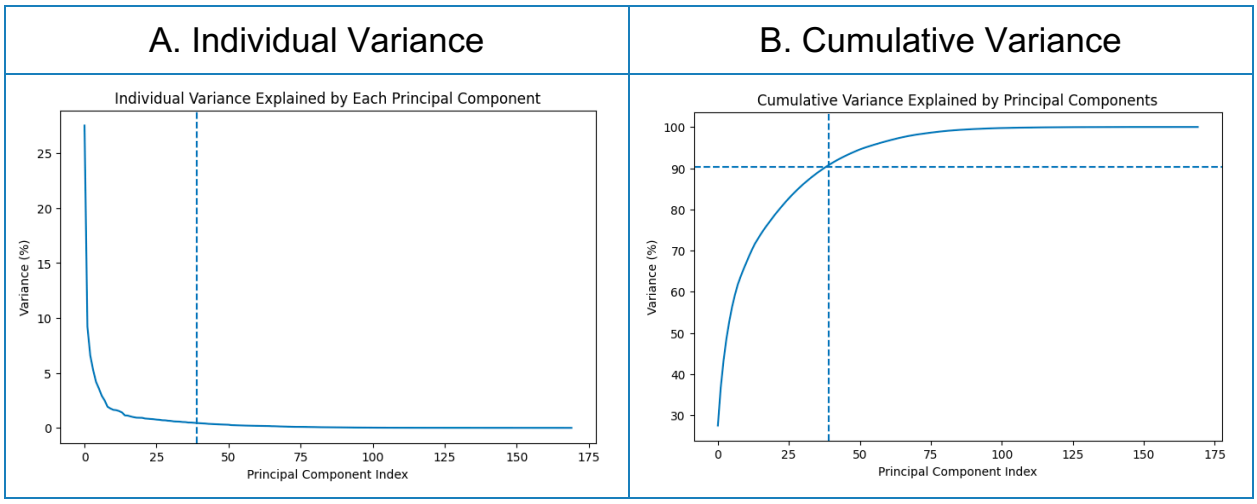

Figure 9. Plots of the individual variance explained by each principal component (A) and the cumulative variance explained by principal components (B).

Four unsupervised dimensionality reduction methods were used to select the 39 principal components that contained the most variance in the extracted features:

- Principal Components Analysis (PCA) with 39 principal components
- Singular Value Decomposition (SVD) with 39 principal components
- Feature Agglomeration (FA) with 39 clusters
- T-distributed Stochastic Neighbor Embedding (TSNE) with 3 components, which is the maximum number of components for TSNE.

G. Classification

Classification methods divide data by labeling them into classes. In this thesis, the classification task was binary to label the data as pathological or physiological. K-Means clustering is a commonly used unsupervised machine learning model to partition a dataset into K distinct clusters. It iteratively assigns data points to the nearest cluster

centroid and updates the centroids based on the mean of the points assigned to each cluster. This process continues until the centroids no longer change significantly or a predetermined number of iterations is reached. The algorithm aims to minimize the within-cluster sum of squares, effectively optimizing the cluster assignments. The aim here was to classify the data into 2 clusters: pathological and physiological.

K-Means and all unsupervised classification methods randomly assign a label (0 or 1) to the two clusters they identify. The Power Spectral Density (PSD) in the 5 major frequency bands, which are the most commonly used features in EEG analysis, were studied in all 71,957 segments to determine how to label the clusters identified by the unsupervised classification models. Figure 10 shows that the median PSDs in the Delta, Alpha, Beta, and Gamma bands in the pathological segments were greater than in the physiological segments. Therefore, after an unsupervised method classified the data into 2 clusters, the sum of the median PSDs in the Delta, Alpha, Beta, and Gamma bands was calculated in each cluster. The cluster with the larger sum was labeled as pathological and the cluster with the smaller sum as physiological.

A. Physio and Patho PSD Medians	B. Patho as a function of Physio
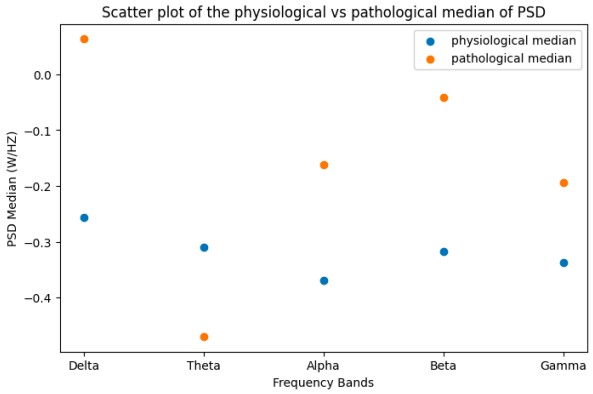	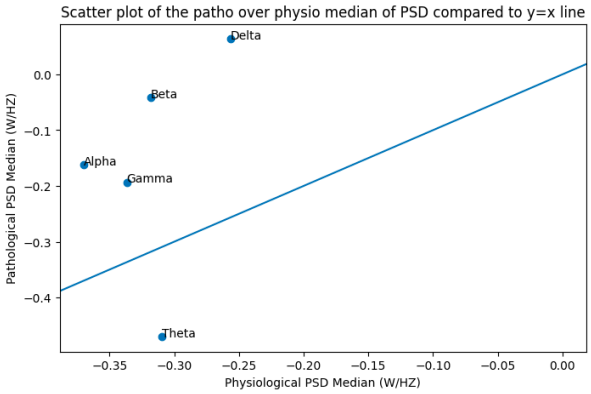

Figure 10. Scatter plot of the physiological and pathological median Power Spectral Densities (PSD) for each one of the 5 major frequency bands (A). Scatter plot of the physiological median PSD as a function of the pathological median PSD for the 5 major frequency bands compared to the y=x line (B).

Four unsupervised classification techniques were combined with the four dimensionality reduction methods to classify each segment as pathological or physiological based on the reduced feature set:

- K-Means
- Gaussian Mixture Model (GMM)
- Hidden Markov Model (HMM)
- One-Class Support Vector Machine (OC SVM)

H. Experimental Paradigms

1. Patient-by-Patient

In a clinical setting, the proposed model would be trained from scratch for each new patient on all of the iEEG data recorded from them. The model would split the data into 3-second segments and classify each of them as pathological or physiological. To reflect how the model would be used in a hospital, each of the 16 model combinations was evaluated by being trained and tested on each one of the 15 patients independently. Before dimensionality reduction and classification, the features were z-score standardized by removing the mean of each feature and scaling to unit variance across each patient's data independently.

2. Cross-Validation

To validate the performance of the unsupervised model, it was compared with two supervised classification methods using a cross-validation paradigm. The 15 patients were split into 5 folds. Each fold was created such that no patient was present in more than one fold and such that the ratio of physiological to pathological segments in the overall dataset of 3.73 was preserved in each fold as best as possible. Table 6 shows, for each fold, the patient assignments by patient ID and, in each fold and in total, the number of physiological and pathological segments and the ratio of physiological to pathological segments.

	Fold 1	Fold 2	Fold 3	Fold 4	Fold 5	Total
Patient ID	0	3	4	5	7	
Patient ID	1	17	8	14	21	
Patient ID	2	23	16	20		
Patient ID			18			
Physiological segments	9,382	8,799	4,093	8,505	25,951	56,730
Pathological segments	2,806	2,747	2,816	3,426	3,432	15,227
Ratio physio over patho	3.34355	3.20313	1.45348	2.48249	7.56148	3.72562

Table 6. 5-fold cross-validation table with the patients assigned to each fold as well as the number of physiological and pathological segments and the ratio of physiological to pathological segments in each fold and in total.

Using this cross-validation paradigm, the best-performing unsupervised model was compared with two supervised classifiers: Support Vector Machine (SVM) and Random Forest. The same dimensionality reduction method from the best-performing unsupervised model was used for SVM and Random Forest.

An SVM separates two classes via an optimal boundary by maximizing the margin between the boundary and the data points closest to it for each class. These points are called support vectors, giving the name Support Vector Machine. An elementary SVM can classify linearly separable classes with a linear equation describing the boundary. For a case such as this application with multiple features, this

boundary was a hyperplane. To address non-linear cases, non-linear kernels can be applied to transform the data into a space where a linear boundary can separate the classes. A linear kernel was used to minimize training time for this binary classification task.

Random Forest is a machine learning algorithm that consists of multiple decision trees where each tree is trained on a random subset of the features. The prediction from all trees is collected to obtain the final prediction, with a reduced variance and limited model overfitting. This algorithm can handle complex data patterns and assess the importance of each feature to classify segments as pathological or physiological.

3. Simulated Data

A simulation model was developed to generate synthetic interictal iEEG brain data that contain pathological epileptic activity. This model simulated pathological activity for various noise levels in the iEEG signal to benchmark test the proposed unsupervised interictal iEEG classifier under different signal noise conditions.

i. iEEG Signal Modeling

To simulate the interictal iEEG brain signal with pathological activity, including HFOs and IEDs, the signal y was modeled as Equation 9.

$$y(t) = \sum_{i=1}^{N_{HFO}} h_i\left(t - t_{h_i}\right) + \sum_{i=1}^{N_{IED}} s_i\left(t - t_{s_i}\right) + \sum_{i=1}^{N_{overlap}} o_i\left(t - t_{o_i}\right) + n(t) \quad \text{[Equation 9]}$$

Where $h_i(t)$ and $s_i(t)$ denote the i[th] HFO and IED event, respectively, in the signal trace at time t_{h_i} and t_{s_i}. $o_i(t)$ denotes the i[th] overlapped event (HFO-IED) in the trace at t_{o_i}. $n(t)$ denotes the noise, and N_{HFO}, N_{IED}, and $N_{overlap}$ denote the total number of individual HFO, individual IED, and overlapped events in signal y, respectively.

ii. Single Event Modeling

A single HFO event, IED event, or overlapped event were modeled as Equation 10, Equation 11, or Equation 12, respectively.

$$h(t) = A_o e^{-\frac{t^2}{2\sigma_o^2}} \cos(2\pi f_o t) \quad \text{[Equation 10]}$$

$$s(t) = (1 - Bt^2) A_s e^{-\frac{t^2}{2\sigma_s^2}}, \ \mathrm{B} = \frac{5}{4\sigma_s^2} \quad \text{[Equation 11]}$$

$$o(t) = h(t) + s(t - t_o) \quad \text{[Equation 12]}$$

Where t_o denotes the time shift between two events. A_o and A_s control the peak amplitude of the HFO and the IED, σ_o and σ_s control the duration of the HFO and the IED (duration = $6 \times \sigma$), and f_o controls the frequency of the HFO.

As shown in Figure 11, the HFO and IED simulations captured the key characteristics of the event. Important features, such as the peak amplitude, duration, and frequency, can be tuned by the model parameters.

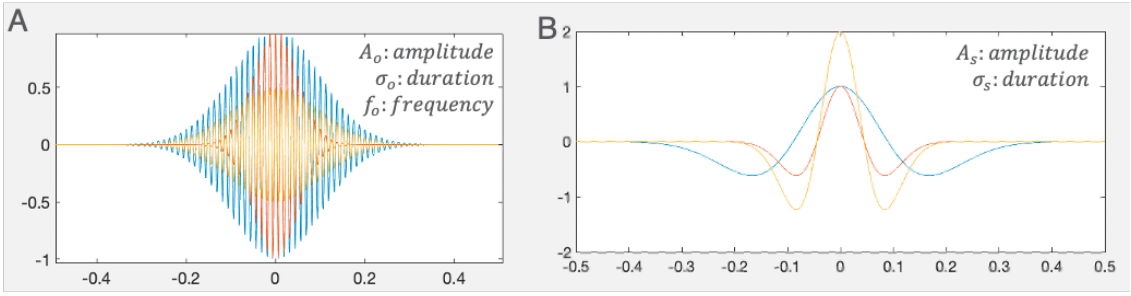

Figure 11. (A) Simulated HFO (Red: A_o=1, σ_o=0.05, f_o=80Hz; Blue: A_o=1, σ_o=0.1, f_o=80Hz; Yellow: A_o=0.5, σ_o=0.1, f_o=80Hz). (B) Simulated IED (Red: A_s=1, σ_s=0.05; Blue: A_s=1, σ_s=0.1; Yellow: A_s=2, σ_s=0.05).

iii. Noise Modeling

For neural signals, it is widely believed that the power spectral density (PSD) of background brain activity follows the power law.[27] The noise $n(t)$ was modeled as brown noise with PSD following the power law as Equation 13.

$$PSD(f) = p * \frac{1}{f^2} \qquad \text{[Equation 13]}$$

Where the noise power p is another tunable parameter that can mimic different noise levels.

iv. Firing Pattern Modeling

To model the firing pattern of HFOs, IEDs, and overlapped events, their inter-event interval (IEI), Δt_{h_i}, Δt_{s_i}, and Δt_{o_i} were modeled as an exponential distribution $exp(\lambda)$, where λ denotes the firing rate, since exponential distribution is a widely used

approximation of stochastic neuronal firing.[28] Figure 12 shows that the real IEI distribution and the simulated exponential IEI distribution are similar.

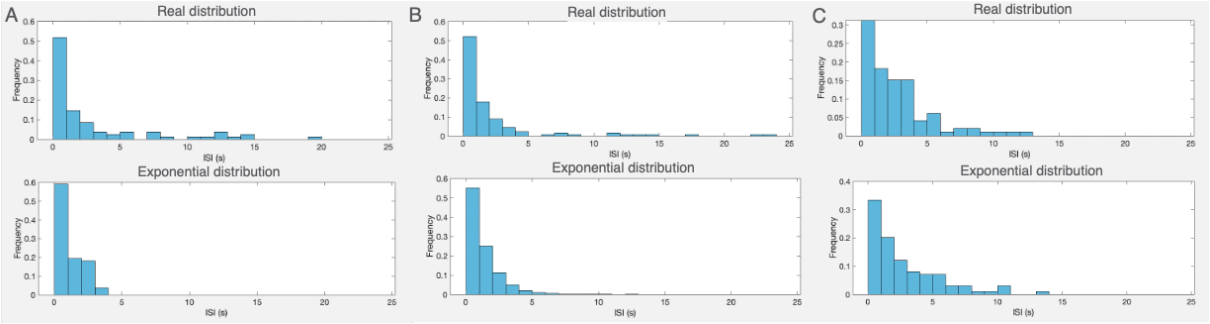

Figure 12. The real signal IEI distribution (top) and exponential distribution (bottom) for (A) ripple (B) fast ripple, and (C) IED. The three λ values correspond to the ripple rate, fast ripple rate, and IED rate. They are the other tunable parameters of this model, which control the density of these events in a simulated signal.

Figure 13 shows examples of four simulated signals with different conditions. Figures 13A and 13B showed the effect of event rates on the signal whereas Figures 13C and 13D showed the effect of noise levels on the signal. As the events rate increased from 0.1/sec (Figure 13A) to 0.5/sec (Figure 13B), the number of events increased from 9 ripples, 12 fast ripples, and 15 IEDs to 46 ripples, 42 fast ripples, and 51 IEDs. As the noise level increased from 10^{-4} W (Figure 13C) to 10^{-3} W (Figure 13D), the noise amplitude in all three event bands increased.

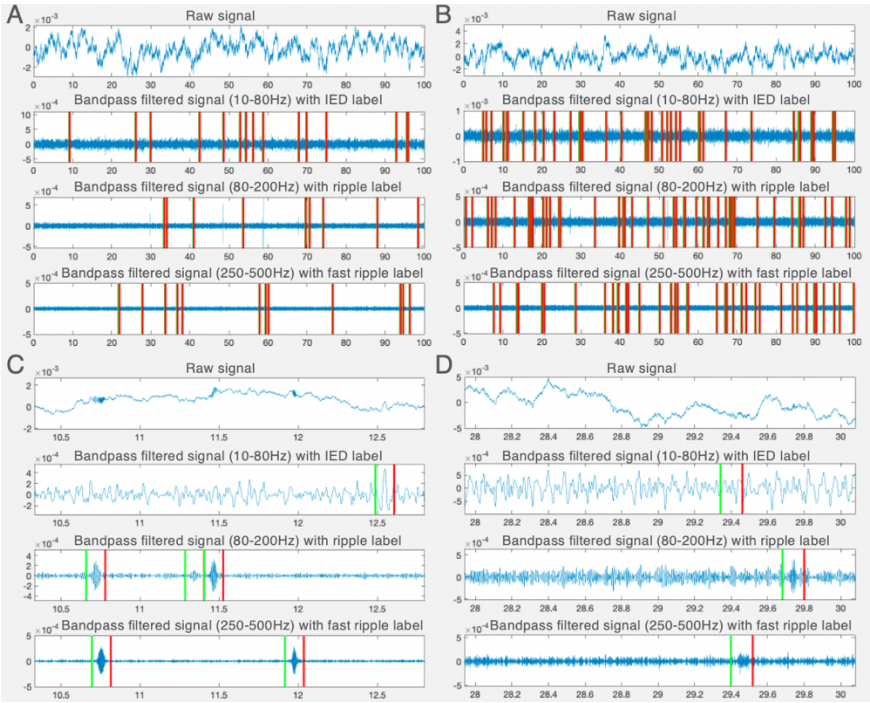

Figure 13. Simulated iEEG signal using different parameters, where the electrophysiological patterns have been marked by green and red vertical lines. In each subfigure, the 1st panel is the raw signal, the 2nd panel is the bandpass filtered signal (10-80Hz) with IED label, the 3rd panel is the bandpass filtered signal (80-200Hz) with ripple label, and the 4th panel is the bandpass filtered signal (250-500Hz) with fast ripple label. The parameters for each subfigure are as follows. Figure A: event rates = 0.1/sec, noise power = 10^{-4} W. Figures B and C: event rates = 0.5/sec, noise power = 10^{-4} W. Figure D: event rates = 0.5/sec, noise power = 10^{-3} W.

v. Simulated Dataset Generation for Benchmark Test

To benchmark test the proposed unsupervised interictal iEEG classifier under different signal noise conditions, a simulated dataset was generated using the synthetic interictal iEEG simulation model. The parameters of single HFO and IED events were

set randomly using a log-normal distribution within a range, as shown in Table 7, to mimic the variations of HFO and IED characteristics in real iEEG recordings.[29-36]

Parameters	Ripple	Fast ripple	IED
Amplitude	100 - 500 μV	100 - 500 μV	100 - 500 μV
Duration	30 - 75 ms	12 - 24 ms	10 - 200 ms
Frequency	80 - 200 Hz	250 - 500 Hz	

Table 7. Amplitude, duration, and frequency parameter ranges for HFOs (ripple and fast ripple) and IEDs used to generate the simulated dataset.

The simulated dataset consisted of 40 iEEG conditions: 2 ripple rates x 2 fast ripple rates x 2 IED rates x 5 noise levels with the corresponding value of each parameter listed in Table 8. For each condition, 100 3-second segments were generated with a 2,000 Hz sampling frequency and simulated 10 times, resulting in 10 groups with 4,000 segments each. Overall, the simulated dataset had 40,000 3-second segments, with 8,000 segments for each of the 5 noise levels.

Ripple rate (/sec)	Fast ripple rate (/sec)	IED rate (/sec)	Noise level (W)	Total number of conditions
0.05, 0.25	0.05, 0.25	0.05, 0.25	10^{-9}, 10^{-8}, 10^{-7}, 10^{-6}, 10^{-5}	40

Table 8. Ripple rate, fast ripple rate, IED rate, and noise level parameters used to generate the simulated dataset.

On top of the noise level in watts (W), noise was also quantified using the signal-to-noise ratio (SNR), which was calculated as the ratio of the power of the synthetically generated iEEG signal over the power of the synthetically generated noise and converted to decibels (dB). The average and range of the SNRs of the 400 conditions in each noise level were calculated and reported in Table 9.

Noise level (W)	Average SNR (dB)	Range of SNR (dB)
10^{-9}	26.99	25.94 – 28.41
10^{-8}	16.97	15.12 – 18.48
10^{-7}	7.03	6.02 – 8.38
10^{-6}	-3.03	-4.63 – -1.17
10^{-5}	-13.02	-14.33 – - 11.66

Table 9. The signal-to-noise ratio's (SNR) average and range for each noise level.

vi. Noise Level-by-Noise Level Paradigm

The 40,000 segments were labeled as 0 or 1. Segments that contained pathological activity, i.e., HFO(s) (ripple or fast ripple) and/or IED(s), were labeled as 1. Segments that did not contain pathological activity were physiological signals and were labeled as 0. There were 19,238 physiological segments and 20,762 pathological segments. Table 10 shows the number of physiological and pathological segments and the ratio of physiological to pathological segments in each noise level and in total. The simulated dataset was well-balanced with a total ratio of physiological to pathological

segments of 0.93, which was consistent across the 5 noise levels and their corresponding SNRs.

Noise level (W)	10^{-9}	10^{-8}	10^{-7}	10^{-6}	10^{-5}	Total
Physiological segments	3,862	3,839	3,857	3,875	3,805	19,238
Pathological segments	4,138	4,161	4,143	4,125	4,195	20,762
Ratio physio over patho	0.93330	0.92261	0.93097	0.93939	0.90703	0.92660

Table 10. Number of pathological and physiological segments and the ratio of physiological to pathological segments in each noise level and in total.

The proposed unsupervised interictal iEEG classifier was evaluated similarly to the patient-by-patient paradigm to benchmark test it under various noise levels. It was trained and tested on the segments from each one of the 5 noise levels independently. Before dimensionality reduction and classification, the features were z-score standardized by removing the mean of each feature and scaling to unit variance across each noise level's data independently. To determine the number of principal components used by the dimensionality reduction method, a threshold of 90% was set for the cumulative variance explained by principal components. This noise level-by-noise level paradigm aimed to identify the noise level threshold over which and the SNR threshold under which the proposed unsupervised model fails to provide classifications that perform better than random chance.

I. Evaluation Metrics

All models were evaluated using three performance metrics: F-2 score, recall, and precision. The F-2 score is a weighted harmonic mean of recall and precision where recall is weighted twice as much as precision. Recall is the ratio of the number of pathological segments correctly classified as pathological to the total number of pathological segments. It quantifies the model's ability to detect pathological segments and is a measure of quantity. Precision is the ratio of the number of pathological segments correctly classified to the total number of segments classified as pathological (either correctly or incorrectly). It quantifies the model's accuracy in classifying a segment as pathological and is a measure of quality.

The proposed model was designed to pre-label interictal iEEG data as an aid to neurologists. The goal of the model is to identify all of the pathological iEEG segments from days' worth of data and provide them for inspection by the clinician. Quantity matters more than quality since the proposed model is not a stand-alone tool and the final classification decision is made by the trained neurologist. Therefore, the performance metric of choice to select the best-performing model was the F-2 score.

The performance metrics used to evaluate the 16 model combinations with the patient-by-patient paradigm were the mean and standard deviation of precision, recall, and F-2 score across the 15 patients. The model with the highest F-2 mean and the lowest F-2 standard deviation was selected as the best-performing combination model.

Similarly, the performance metrics used in the cross-validation paradigm were the mean and standard deviation of precision, recall, and F-2 score across the 5 cross-validation folds. The performance metric used in the noise level-by-noise level paradigm was the F-2 score across the segments in each of the 5 noise levels.

J. Statistical Analysis

After evaluating the best-performing unsupervised model and the two supervised models, the one-way analysis of variance (ANOVA) test was used to test whether there was a significant difference between the F-2 score means of the three models at the 0.05 alpha level. The null hypothesis was that the three F-2 score means were equal.

This one-way ANOVA test had three assumptions: the F-2 scores for each model were assumed to be independent, the F-2 scores for each model were assumed to have a normal distribution, and these three distributions were assumed to have equal variance. The Shapiro-Wilk test was used to test for normality in the F-2 scores for each model at the 0.05 significance level. The null hypothesis was that the F-2 scores were normally distributed. The Bartlett test, which assumed normality, was used to determine whether the variances of the three F-2 score distributions were equal at the 0.05 alpha level. The null hypothesis was that the three F-2 score distributions' variances were equal.

III. Results

A. Patient-by-Patient Paradigm

Table 11 shows the performance comparison of the 16 model combinations across 15 patients by their F-2 score mean and standard deviation, precision mean and standard deviation, and recall mean and standard deviation. The combination of PCA with K-Means performed best with a 92.6% average F-2 score and a 12.0% F-2 score standard deviation. It also achieved an average of 93.5% precision and 93.0% recall with a 13.8% precision standard deviation and 12.5% recall standard deviation. PCA + K-Means achieved the highest average F-2 score and the lowest F-2 score standard deviation as well as the highest average recall score and the lowest recall standard deviation out of all 16 model combinations. Although the combinations of TSNE with K-Means and PCA with GMM performed almost as well, PCA combined with K-Means had lower standard deviations for F-2 score and recall and may thus be the most generalizable model. On top of that, PCA is less computationally expensive and faster than TSNE, which does not scale well with large datasets the proposed model will have to deal with when used in clinical settings. A flowchart of the final overall proposed model is presented in Figure 14.

Model Combination	F-2 score mean	F-2 score standard deviation	Precision mean	Precision standard deviation	Recall mean	Recall standard deviation
PCA + K-Means	**0.926211**	**0.119791**	0.934989	0.137673	0.929816	0.125025
TSNE + K-Means	0.925209	0.150149	0.954348	0.110529	0.921792	0.160205
PCA + GMM	0.923016	0.145347	0.938190	0.126900	0.922956	0.152048
FA + K-Means	0.915365	0.146197	0.967233	0.068251	0.907236	0.162571
SVD + K-Means	0.915177	0.146877	0.951017	0.116250	0.910862	0.158736
SVD + GMM	0.913556	0.148946	0.967338	0.068533	0.905239	0.165602
SVD + HMM	0.904725	0.140749	0.929200	0.131768	0.902398	0.148991
TSNE + GMM	0.895694	0.171208	0.933219	0.134776	0.890317	0.181003
FA + GMM	0.889879	0.160397	0.94561	0.116116	0.883352	0.177091
FA + HMM	0.886863	0.143524	0.934919	0.121783	0.87958	0.155568
FA + OC SVM	0.872724	0.185131	0.965267	0.078902	0.858832	0.204956
SVD + OC SVM	0.872477	0.185448	0.965360	0.078290	0.858538	0.205333
PCA + HMM	0.871250	0.183383	0.944420	0.121684	0.861650	0.199397
PCA + OC SVM	0.870789	0.188116	0.970390	0.063846	0.855914	0.209177
TSNE + OC SVM	0.835245	0.205759	0.969443	0.056738	0.816177	0.229154
TSNE + HMM	0.834625	0.207534	0.968798	0.064828	0.815473	0.230641

Table 11. Performance metrics for the 16 model combinations ranked by F-2 score mean.

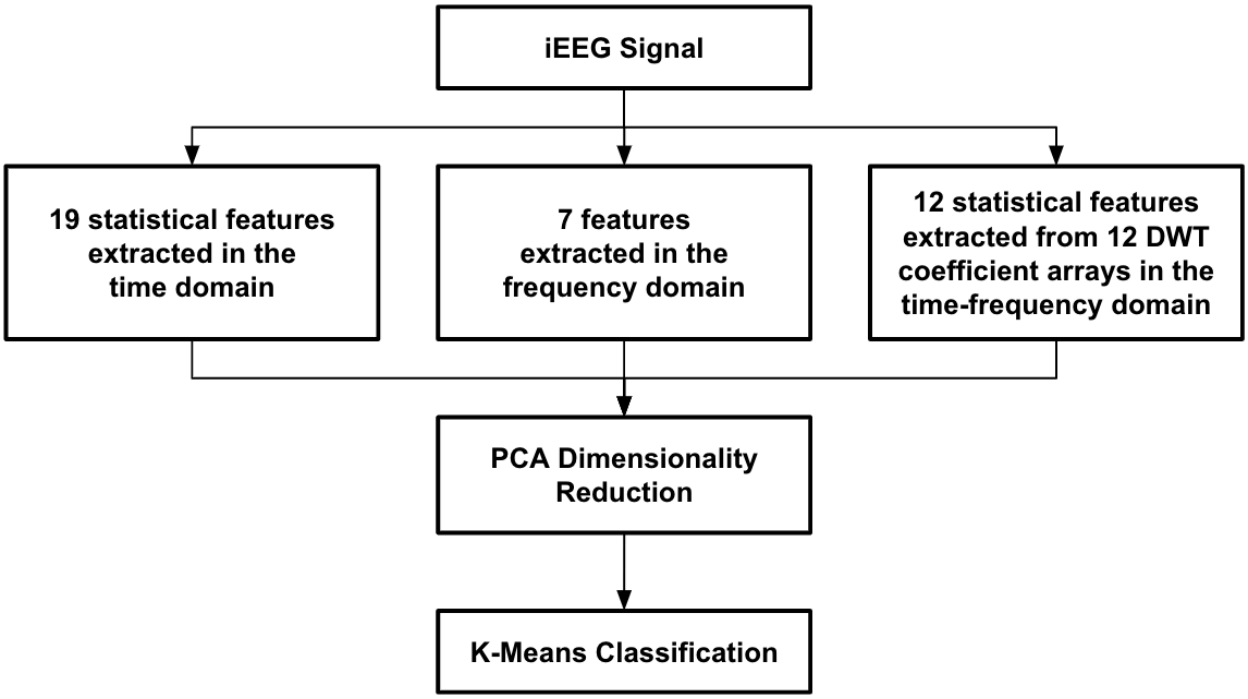

Figure 14. Flowchart of the proposed unsupervised interictal iEEG activity classification model.

B. Cross-Validation Paradigm

1. Model Performance

PCA combined with K-Means was the best-performing unsupervised model. The SVM and Random Forest supervised classifiers were also combined with PCA to reduce the dimensionality to 39 principal components. Figure 15 shows a bar graph comparison of the F-2 score mean and standard deviation for the three models. Table 12 shows the detailed performance comparison of the K-Means, SVM, and Random Forest models across 5 cross-validation folds by their F-2 score mean and standard deviation, precision mean and standard deviation, and recall mean and standard deviation. K-Means performed best with a 72.9% average F-2 score and a 6.8% F-2

score standard deviation. K-means also achieved the highest average recall with 74.4% and the lowest recall standard deviation with 8.7%. That said, SVM achieved a similar performance with a 72.4% average F-2 score (12.5% F-2 score standard deviation) and a 74.0% average recall (16.7% F-2 score standard deviation) while achieving a higher average precision (71.9%) than K-Means (69.3%). Random Forest did not perform as well for the F-2 score and recall but achieved the highest average precision of 80.0%. K-Means may also be the most generalizable model of the three as it achieved a lower standard deviation in all three performance metrics, with half the standard deviation of the two supervised models for the F-2 score and recall.

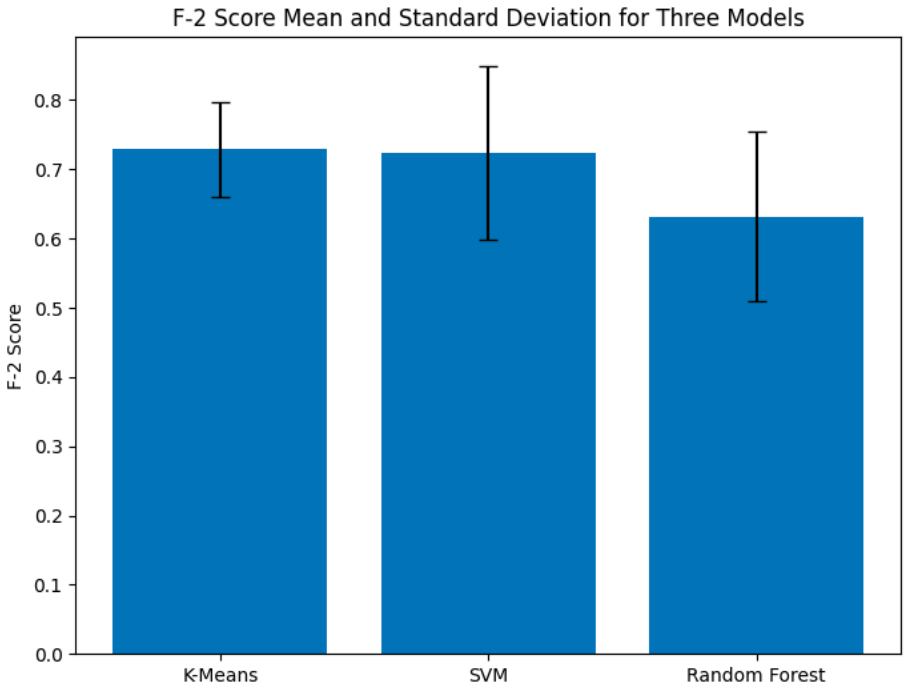

Figure 15. Bar graph of the F-2 score mean and standard deviation for the proposed unsupervised model and two supervised models.

Model	F-2 score mean	F-2 score standard deviation	Precision mean	Precision standard deviation	Recall mean	Recall standard deviation
K-Means	0.728642	0.067707	0.692807	0.100147	0.743587	0.086765
SVM	0.723720	0.124758	0.719189	0.142703	0.740149	0.167377
Random Forest	0.631625	0.122313	0.800173	0.121862	0.608815	0.156734

Table 12. Performance metrics for the proposed unsupervised model and two supervised models.

2. Statistical Analysis

The F-2 scores were independent since they were obtained from 5 independent groups of independent patients' data. The Shapiro-Wilk test yielded p-values of 0.7818, 0.5988, and 0.0707 for the K-Means, SVM, and Random Forest F-2 scores, respectively. All three p-values were greater than 0.05. The null hypothesis of normally distributed F-2 scores was not rejected for all three models, concluding that the F-2 scores had a normal distribution for each model at the 0.05 alpha level. The Bartlett test yielded a p-value of 0.4811, which was greater than 0.05. The null hypothesis of equal variances was not rejected, concluding that the three F-2 score distributions' variances were equal at the 0.05 significance level. All three assumptions to use a one-way ANOVA test were satisfied.

The one-way ANOVA test yielded a p-value of 0.3145, which was greater than 0.05. The null hypothesis of equal means was not rejected. This result showed no significant difference between the F-2 score means of the three models at the 0.05 alpha level.

C. Noise Level-by-Noise Level Paradigm with Simulated Dataset

The threshold of 90% for the cumulative variance explained by principal components using PCA resulted in 27 principal components, which explained 90.1% of the variance. After the features in the time, frequency, and time-frequency domains were extracted from the simulated dataset, PCA was used to reduce the dimensionality to 27 principal components and combined with K-Means to classify segments as pathological or physiological. Figure 16 shows the F-2 score was the highest at 85.8% for the lowest level of noise of 10^{-9} W and the highest SNR of 26.99 dB. The F-2 score was lower for 10^{-8} W/16.97 dB at 71.9% and reached a plateau of 51.2% at noise levels of 10^{-7}, 10^{-6}, and 10^{-5} W and SNRs of 7.03, -3.03, and -13.02 dB. At noise levels greater than or equal to the threshold of 10^{-7} W and SNRs less than or equal to the threshold of 7.03 dB, the proposed unsupervised model failed to provide classifications that performed better than random chance.

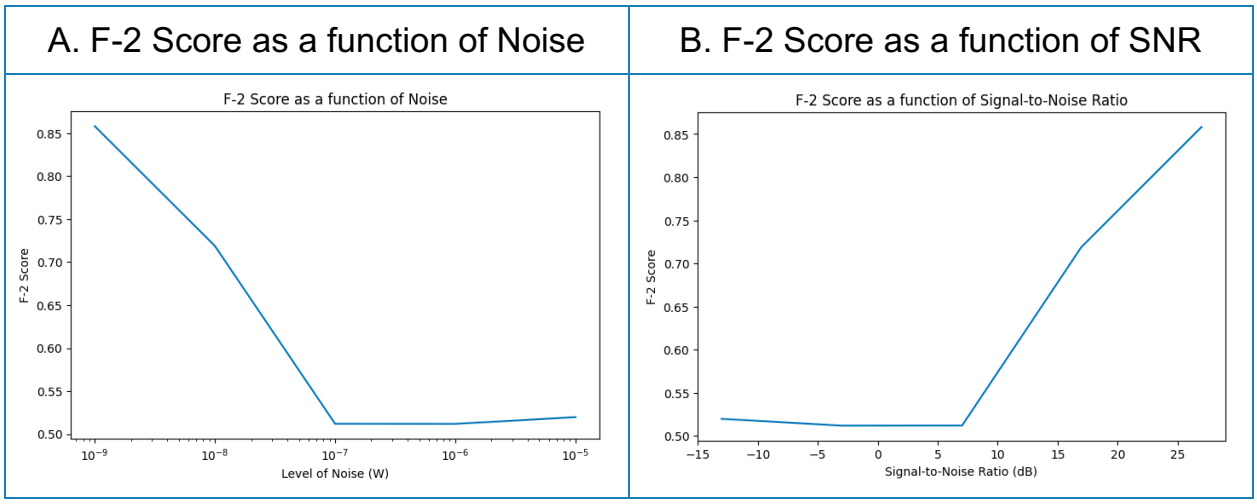

Figure 16. Plots of the F-2 score for each of the 5 noise levels (A) and each of the 5 signal-to-noise ratios (SNR) (B) in the iEEG simulated dataset.

IV. Discussion

The primary objective of this research was to develop and validate an unsupervised model for classifying interictal iEEG activity in epilepsy patients as pathological or physiological. This model aims to enhance the efficiency of localizing the SOZ for faster treatment and shorter hospital length of stay for patients who do not respond to anti-seizure medications.

A. Model Performance and Implications

Based on the metric of choice for evaluation, the F-2 score, PCA for dimensionality reduction combined with K-Means for classification was the best-performing model out of 16 model combinations. This proposed model achieved an average F-2 score of 92.6%, with a precision of 93.5% and recall of 93.0%. This performance, coupled with the lowest standard deviations across F-2 score and recall, suggests that PCA combined with K-Means is highly effective, stable, and more generalizable than other unsupervised model combinations.

The superiority of PCA + K-Means is further highlighted when considering computational efficiency. PCA is less computationally intensive than techniques like TSNE, making it more suitable for clinical settings where quick data processing is essential. This speed, along with high performance, positions PCA + K-Means as a

viable tool for real-time analysis of iEEG data, potentially reducing the workload on neurologists and improving the speed of SOZ localization.

B. Cross-Validation and Statistical Analysis

The cross-validation paradigm further confirmed the robustness of the unsupervised PCA + K-Means model by comparing it to two supervised models: SVM and Random Forest. Despite the slightly higher precision of the Random Forest model, the unsupervised K-Means model demonstrated superior F-2 score and recall and lower standard deviations than SVM and Random Forest across all three performance metrics, underscoring the reliability and generalizability of PCA + K-Means. The data collection and processing and the statistical analysis using the Shapiro-Wilk and Bartlett tests confirmed that the assumptions for independence, normality, and equal variances were met, justifying the use of one-way ANOVA for comparing the three models' performances. The one-way ANOVA results indicated no statistically significant difference between the F-2 score means of the models, reinforcing the competitive performance of the unsupervised approach. The proposed model, without relying on any labels for training, did not perform significantly differently than the two supervised models, which relied on labels to learn patterns in the iEEG data relevant to pathological activity.

C. Noise Resilience

The model's resilience to noise was evaluated using a simulated dataset of iEEG brain activity. The results indicated that the lower the noise level and the higher the SNR, the better the PCA + K-Means model performs. It achieved an F-2 score of 85.8% at a 10^{-9} W noise level and 26.99 dB SNR but as the noise level increased and SNR decreased, the model's performance degraded, reaching a plateau around 51.2% at noise levels of 10^{-7} W and above and SNRs of 7.03 dB and below. This finding suggests that while the model is effective, its performance may be compromised in noisier data environments with a noise threshold of 10^{-7} W and SNR threshold of 7.03 dB, a limitation to be addressed in future work.

In a 2009 study, 4 epilepsy patients were subdurally implanted with iEEG grid electrodes in motor and pre-frontal cortical regions.[37] The average SNR in the motor cortical regions across the 4 patients was 19.07 dB and ranged from 13.47 to 26.28 dB. The average SNR in the pre-frontal cortical regions across the 4 patients was 2.86 dB and ranged from 2.22 to 4.37 dB. Based on these values of the SNRs in iEEG recordings, the proposed model may not be effective in all clinical environments. This noise limitation was expected as the model was developed for data that included no power line noise or muscle and machine artifacts.

D. Clinical Implications

The proposed unsupervised model holds significant promise for clinical application. It overcomes the tedious, time-consuming, and unscalable limitations of the manual detection of pathological activity by automatically performing analysis and classification of iEEG data. It can assist neurologists in identifying pathological data segments, thereby streamlining the review process and improving the efficiency of SOZ localization. This capability is crucial for patients undergoing lengthy Video-EEG Monitoring (VEM), where vast amounts of iEEG data are recorded but only a fraction is analyzed due to time constraints.

On top of that, the proposed method tackles the shortcomings of supervised algorithms since it offers a new and personalized model for every new patient who comes into the clinic. It is trained from scratch on their brain data as soon as the data are collected, skipping the time-consuming and expensive labeling process by trained neurologists. This adaptability is essential for personalized medicine, allowing the model to provide tailored insights based on each patient's unique brain activity patterns.

E. Limitations

This thesis has a few limitations. No hyperparameter tuning was performed for the unsupervised and supervised classification models. For example, the SVM model

was used with a linear kernel but may perform better with different kernels, such as the radial basis function.

The patient sample size of 15 was not large, making it necessary to validate the proposed model externally on a different clinical dataset. Although a separate dataset was used to explore the noise limitations of the proposed model, the simulated data was synthetic. This noise limitation was studied and quantified, which led to the finding that the model fails to perform better than random chance above the 10^{-7} W noise level threshold and below the 7.03 dB SNR threshold.

F. Future Directions

There are several future directions to further this work. It is important to apply the proposed model to external clinical iEEG datasets, such as the publicly available St. Anne's University Hospital dataset, to validate the model's effectiveness and usability across different epilepsy cases recorded in diverse clinical settings.[15]

To optimize the model's performance, hyperparameter tuning and identifying the most clinically relevant evaluation metric are necessary. Seeking epileptologists' feedback for what they look for would help tailor a model that best complements and fits into their clinical workflow. Getting their perspective on the F-2 score as the metric of choice would be useful to inform which performance metric the model assessment should be based on.

Improving the resilience to noise would also make the proposed model more robust. This could be accomplished by adding a filtering step with a notch filter at 60 Hz to remove power line noise and additional filters to remove muscle and machine artifacts.

Another significant step to improve the proposed model's performance would be compiling a large dataset of all publicly available iEEG data from epilepsy patients. This dataset would be composed of both labeled and unlabeled available datasets, although labels would be removed. When a new patient goes through VEM in the hospital, the patient's unlabeled iEEG data would be added to the large unlabeled dataset. The proposed unsupervised PCA + K-Means model would be trained on this large dataset that includes the new patient's data. This large unsupervised model would then classify the patient's data segments as pathological or physiological. Within a hospital system, the unlabeled dataset would be growing continuously as more patients come in. The proposed PCA + K-Means model would be trained from scratch after every new patient's data is collected and added to the large dataset before automatically classifying their data. Integrating this model into clinical workflows could provide neurologists with a powerful tool for managing and treating drug-resistant epilepsy more efficiently.

V. Conclusion

This thesis presented a fully automated and personalized algorithm leveraging unsupervised learning to classify interictal iEEG activity as pathological or physiological in epilepsy patients. The development of this unsupervised model for interictal pathological activity detection represents a significant advancement in epilepsy research. The proposed model extracted features in the time, frequency, and time-frequency domains. It then performed unsupervised dimensionality reduction using PCA and unsupervised classification of each iEEG 3-second segment using K-Means. Without labeled data, the model performed similarly to supervised models, which relied on labels, and achieved an average F-2 score of 92.6%, an average precision of 93.5%, and an average recall of 93.0% across 15 epilepsy patients. The proposed model demonstrated high performance with great potential to be used clinically by neurologists to make the most of all of the data recorded during video-EEG monitoring, thereby offering a promising approach to improving the efficiency of treatment for drug-resistant epilepsy.

Bibliography

1. “Who Can Get Epilepsy?” *Epilepsy Foundation*, https://www.epilepsy.com/what-is-epilepsy/understanding-seizures/who-gets-epilepsy.

2. “Epilepsy.” *World Health Organization*, World Health Organization, https://www.who.int/news-room/fact-sheets/detail/epilepsy.

3. James Tao, MD. “New Treatment Options for Drug-Resistant Epilepsy.” New Treatment Options for Drug-Resistant Epilepsy - UChicago Medicine, UChicago Medicine, 5 Dec. 2022, www.uchicagomedicine.org/forefront/neurosciences-articles/new-treatment-options-for-people-with-drug-resistant-epilepsy#:~:text=Most%20of%20these%20people%20are,to%20standard%20anti%2Dseizure%20medications.

4. “EEG (Electroencephalogram).” Mayo Clinic, Mayo Foundation for Medical Education and Research, 11 May 2022, https://www.mayoclinic.org/tests-procedures/eeg/about/pac-20393875.

5. Chan, Alvin Y., et al. “Length of stay for patients undergoing invasive electrode monitoring with stereoelectroencephalography and subdural grids correlates positively with increased institutional profitability.” Epilepsia, vol. 58, no. 6, 2017, pp. 1023–1026, https://doi.org/10.1111/epi.13737.

6. Shah, AashitK, and Sandeep Mittal. “Invasive electroencephalography monitoring: Indications and presurgical planning.” Annals of Indian Academy of Neurology, vol. 17, no. 5, 2014, p. 89, https://doi.org/10.4103/0972-2327.128668.

7. Saminu, Sani, et al. “A Recent Investigation on Detection and Classification of Epileptic Seizure Techniques Using EEG Signal.” Brain Sciences, vol. 11, no. 5, 2021, p. 668., https://doi.org/10.3390/brainsci11050668.

8. Dewar, Sandra R., and Mimi Callanan. "Nursing Practice in a Video-EEG Monitoring Unit." Atlas of Video-EEG Monitoring Eds. Joseph I. Sirven, and John M. Stern. McGraw Hill, 2011, https://neurology.mhmedical.com/content.aspx?bookid=1045&sectionid=59103051.

9. Jiang, Haiteng, et al. “Interictal SEEG Resting-State Connectivity Localizes the Seizure Onset Zone and Predicts Seizure Outcome.” Advanced Science, vol. 9, no. 18, 2022, p. 2200887., https://doi.org/10.1002/advs.202200887.

10. Hartshorn, Alendia, and Barbara Jobst. “Responsive Brain Stimulation in Epilepsy.” Therapeutic Advances in Chronic Disease, vol. 9, no. 7, 2018, pp. 135–142., https://doi.org/10.1177/2040622318774173.

11. Fedele, Tommaso, et al. “Resection of high frequency oscillations predicts seizure outcome in the individual patient.” Scientific Reports, vol. 7, no. 1, 23 Oct. 2017, https://doi.org/10.1038/s41598-017-13064-1.

12. Papadelis, Christos, et al. “Interictal High Frequency Oscillations Detected with Simultaneous Magnetoencephalography and Electroencephalography as Biomarker of Pediatric Epilepsy.” Journal of Visualized Experiments, no. 118, 2016, https://doi.org/10.3791/54883.

13. Saminu, Sani, et al. “A Recent Investigation on Detection and Classification of Epileptic Seizure Techniques Using EEG Signal.” Brain Sciences, vol. 11, no. 5, 2021, p. 668., https://doi.org/10.3390/brainsci11050668.

14. Gardner, Andrew B., et al. “One-Class Novelty Detection for Seizure Analysis from Intracranial EEG.” Journal of Machine Learning Research, 2006, pp. 1025–44, www.seas.upenn.edu/~littlab/Site/Publications_files/gardner%20JMLR%202006.pdf.

15. Nejedly, Petr, et al. “Multicenter Intracranial EEG Dataset for Classification of Graphoelements and Artifactual Signals.” *Scientific Data*, vol. 7, no. 1, 2020, https://doi.org/10.1038/s41597-020-0532-5.

16. Kong, Qingkai, et al. “Chapter 24 - Fourier Transform.” *Python Programming and Numerical Methods: A Guide for Engineers and Scientists*, Academic Press, London, 2021.

17. Welch, P. “The Use of Fast Fourier Transform for the Estimation of Power Spectra: A Method Based on Time Averaging over Short, Modified Periodograms.” IEEE Transactions on Audio and Electroacoustics, vol. 15, no. 2, 1967, pp. 70–73., https://doi.org/10.1109/tau.1967.1161901.

18. Nunez, Paul L. “Electroencephalography (EEG).” Encyclopedia of the Human Brain, 2002, pp. 169–179., https://doi.org/10.1016/b0-12-227210-2/00128-x.

19. Von Bünau Paul, et al. “Finding Stationary Brain Sources in EEG Data.” 2010 Annual International Conference of the IEEE Engineering in Medicine and Biology, 2010, https://doi.org/10.1109/iembs.2010.5626537.

20. Kehtarnavaz, Nasser. “Frequency Domain Processing.” *Digital Signal Processing System Design*, 2008, pp. 175–196., https://doi.org/10.1016/b978-0-12-374490-6.00007-6.

21. Huang, Bi-Ling, and Yuan Yao. “Batch-to-Batch Steady State Identification via Online Ensemble Empirical Mode Decomposition and Statistical Test.” *Computer Aided Chemical Engineering*, 2014, pp. 787–792., https://doi.org/10.1016/b978-0-444-63456-6.50132-0.

22. Furht, Borko. “Discrete Wavelet Transform (DWT).” *Encyclopedia of Multimedia*, 2008, pp. 188–188., https://doi.org/10.1007/978-0-387-78414-4_305.

23. Akansu, Ali N., and Richard A. Haddad. “Wavelet Transform.” *Multiresolution Signal Decomposition*, 2001, pp. 391–442., https://doi.org/10.1016/b978-012047141-6/50006-9.

24. Makowski, Dominique, et al. “NeuroKit2: A python toolbox for Neurophysiological Signal Processing.” Behavior Research Methods, vol. 53, no. 4, 2 Feb. 2021, pp. 1689–1696, https://doi.org/10.3758/s13428-020-01516-y.

25. Makowski, Dominique, et al. “Neurophysiological Data Analysis with Neurokit2.” Neurophysiological Data Analysis with NeuroKit2 - NeuroKit2 0.2.10 Documentation, 2021, https://neuropsychology.github.io/NeuroKit/.

26. Lei, Yaguo. “Signal Processing and Feature Extraction.” *Intelligent Fault Diagnosis and Remaining Useful Life Prediction of Rotating Machinery*, 2017, pp. 17–66., https://doi.org/10.1016/b978-0-12-811534-3.00002-0.

27. Miller, Kai J., et al. “Power-law scaling in the brain surface electric potential.” PLoS Computational Biology, vol. 5, no. 12, 18 Dec. 2009, https://doi.org/10.1371/journal.pcbi.1000609.

28. Burkitt, A. N. “A review of the integrate-and-fire neuron model: I. Homogeneous synaptic input.” Biological Cybernetics, vol. 95, no. 1, 19 Apr. 2006, pp. 1–19, https://doi.org/10.1007/s00422-006-0068-6.

29. Jiruska, Premysl, et al. “Update on the mechanisms and roles of high-frequency oscillations in seizures and epileptic disorders.” Epilepsia, vol. 58, no. 8, 6 July 2017, pp. 1330–1339, https://doi.org/10.1111/epi.13830.

30. de Curtis, Marco, et al. “Interictal Epileptiform Discharges in Partial Epilepsy: Complex Neurobiological Mechanisms Based on Experimental and Clinical Evidence.” Jasper's Basic Mechanisms of the Epilepsies, edited by Jeffrey L Noebels et. al., 4th ed., National Center for Biotechnology Information (US), 2012.

31. Abd El-Samie, Fathi E., et al. “A review of EEG and Meg epileptic spike detection algorithms.” IEEE Access, vol. 6, 2018, pp. 60673–60688, https://doi.org/10.1109/access.2018.2875487.

32. Tingley, David, and György Buzsáki. “Routing of hippocampal ripples to subcortical structures via the lateral septum.” Neuron, vol. 105, no. 1, Jan. 2020, https://doi.org/10.1016/j.neuron.2019.10.012.

33. Fedele, Tommaso, et al. “Resection of high frequency oscillations predicts seizure outcome in the individual patient.” Scientific Reports, vol. 7, no. 1, 23 Oct. 2017, https://doi.org/10.1038/s41598-017-13064-1.

34. Jing, Jin, et al. “Interrater reliability of experts in identifying interictal epileptiform discharges in Electroencephalograms.” JAMA Neurology, vol. 77, no. 1, 1 Jan. 2020, p. 49, https://doi.org/10.1001/jamaneurol.2019.3531.

35. Aanestad, Eivind, et al. “Interictal epileptiform discharges vary across age groups.” Clinical Neurophysiology, vol. 131, no. 1, Jan. 2020, pp. 25–33, https://doi.org/10.1016/j.clinph.2019.09.017.

36. Kural, Mustafa Aykut, et al. “Criteria for defining interictal epileptiform discharges in EEG.” Neurology, vol. 94, no. 20, 19 May 2020, https://doi.org/10.1212/wnl.0000000000009439.

37. Ball, Tonio, et al. “Signal quality of simultaneously recorded invasive and non-invasive EEG.” NeuroImage, vol. 46, no. 3, July 2009, pp. 708–716, https://doi.org/10.1016/j.neuroimage.2009.02.028.